Supporting information

Structurally Engineered $ZnCo_2O_4$ Spinel Nanoparticles on ZIF-derived Hierarchically Porous Graphitic Carbon for High-Performance Flow Capacitive Deionization

Swayamprakash Biswal[†], Biswajit Mishra[†], and Bijay P. Tripathi[*]

Functional Materials and Membranes Laboratory, Department of Materials Science and Engineering, Indian Institute of Technology Delhi, Hauz Khas, New Delhi, 110016, India.

†Equal contributions

Table of Contents

S1. Materials and Methodologies *S3*

S1.1. Materials S3

S1.2. Synthesis of flow electrodes S3

S1.2.1. Synthesis of Zn/Co ZIF S3

S1.2.2. Synthesis of $ZnCo_2O_4$@GPC S3

S1.2.3. Synthesis of Co_3O_4@GPC S4

S1.2.4. Synthesis of GPC S4

S1.3. Instrumentation S4

S1.4. Electrochemical performance S5

S1.5. Flow capacitive deionization performance S6

S2. Structural and Morphological Characterizations *S8*

S2.1. FESEM analysis of Zn/Co-ZIF S8

S2.2. FESEM analysis of Zn/CoNP@GPC S8

S2.3. FESEM analysis of $ZnCo_2O_4$@GPC S9

S2.4. HRTEM analysis of Zn/Co-ZIF S9

S2.5. HRTEM analysis of Zn/CoNP@GPC S10

S2.6. XPS survey spectra analysis comparison S10

S3. Additional information about FCDI performance *S11*

S3.1. FCDI performance of Zn/CoNP@GPC S11

S3.2. XRD analysis and FCDI performance of Co_3O_4@GPC S11

S3.3. Structural characterization, surface property and FCDI performance analysis of GPC and ZIF-8 and AC S12

S3.5. FCDI performance by varying applied potential S13

S3.6. FCDI performance by varying feed salt concentration S15

S3.7. EIS analysis of $ZnCo_2O_4$ and all control samples S16

S4. Post-FCDI structural and morphological analysis..... S17

Table S1: Comparative study of the desalination performance of flow-electrode with previously reported literatures. S18

References: S19

S1. Materials and Methodologies

S1.1. Materials

Zinc nitrate hexahydrate ($Zn(NO_3)_2 \cdot 6H_2O$, ≥98%), cobalt nitrate hexahydrate ($Co(NO_3)_2 \cdot 6H_2O$, ≥98%), and 2-methylimidazole (99%) were purchased from Sigma-Aldrich and used as received without further purification. Cetyltrimethylammonium bromide (≥99%) was obtained from Merck and employed as a surfactant during ZIF synthesis. Ethanol (99.9%) and N,N-dimethylformamide (DMF, anhydrous) were acquired from Fisher Scientific. All aqueous solutions were prepared using deionized (DI) water with a resistivity of 18.2 MΩ·cm obtained from a Milli-Q water purification system. Commercial activated carbon (AC) used for comparative studies was obtained from Sigma-Aldrich. All chemicals were of analytical grade and used without any additional treatment.

S1.2. Synthesis of flow electrodes

S1.2.1. Synthesis of Zn/Co ZIF

The bimetallic Zn/Co-ZIF precursor was synthesized following a previously reported method with minor modifications.[1] Zinc nitrate hexahydrate (1.25 mmol, 0.37 g) and cobalt nitrate hexahydrate (2.5 mmol, 0.72 g) were dissolved in 150 mL of methanol under magnetic stirring. Cetyltrimethylammonium bromide (CTAB, 0.25 g) was added to the solution to act as a surfactant, assisting in particle size control and porosity modulation. In a separate container, 2-methylimidazole (40 mmol, 3.3 g) was dissolved in 150 mL of methanol. The ligand solution was rapidly added to the metal solution under vigorous stirring to initiate ZIF formation. The reaction mixture was stirred continuously for 24 hours at room temperature to allow for complete coordination and crystallization. A purple precipitate formed during this time, indicating successful incorporation of both Zn^{2+} and Co^{2+} into the ZIF framework. The solid product was collected by centrifugation at 7000 rpm for 5 minutes, washed thoroughly with methanol three times to remove unreacted species and residual CTAB, and dried under vacuum at room temperature overnight. The resulting Zn/Co-ZIF powder was used as a precursor for subsequent thermal transformation steps.

S1.2.2. Synthesis of $ZnCo_2O_4$@GPC

The $ZnCo_2O_4$@GPC composite was synthesized via a two-step thermal transformation of the as-prepared Zn/Co-ZIF precursor. In the first step, the Zn/Co-ZIF powder was placed in a ceramic boat and subjected to pyrolysis under a nitrogen atmosphere. The sample was heated to 700 °C at a ramp rate of 3 °C min^{-1} and held at this temperature for 2 h to ensure complete

carbonization of the organic ligands and formation of nitrogen-doped graphitic carbon. During this process, the metal ions were partially reduced to metallic nanoparticles or dispersed within the carbon matrix, resulting in an intermediate material denoted as Zn/CoNP@GPC. In the second step, the Zn/CoNP@GPC powder was transferred to a muffle furnace and calcined in air at 350 °C for 1 h with a heating rate of 3 °C min^{-1}. This mild oxidation treatment converted the cobalt species into crystalline $ZnCo_2O_4$ spinel nanoparticles while preserving the conductive carbon framework. The final product, referred to as $ZnCo_2O_4$@GPC, was collected as a dark powder and stored for further characterization and application in FCDI experiments.

S1.2.3. Synthesis of Co_3O_4@GPC

The Co_3O_4@GPC composite was synthesized via a two-step thermal transformation of the as-prepared ZIF-67 precursor.[2] In the first step, the ZIF-67 powder was placed in a ceramic boat and subjected to pyrolysis under a nitrogen atmosphere. The sample was heated to 700 °C at a ramp rate of 3 °C min^{-1} and held at this temperature for 2 h to ensure complete carbonization of the organic ligands and formation of nitrogen-doped graphitic carbon. During this process, the metal ions were partially reduced to metallic nanoparticles or dispersed within the carbon matrix, resulting in an intermediate material denoted as CoNP@GPC. In the second step, the CoNP@GPC powder was transferred to a muffle furnace and calcined in air at 350 °C for 1 h with a heating rate of 3 °C min^{-1}. This mild oxidation treatment converted the cobalt species into crystalline Co_3O_4 spinel nanoparticles while preserving the conductive carbon framework. The final product, referred to as Co_3O_4@GPC, was collected as a dark powder and stored for further characterization and application in FCDI experiments.

S1.2.4. Synthesis of GPC

For the synthesis of GPC, the ZIF-8 precursor was synthesized via the reported synthesis method.[3] Following that, a pyrolytic treatment of ZIF-8 precursor was performed by heating the sample at 900 °C at a ramp rate of 3 °C min^{-1} and held at this temperature for 2 h to ensure complete carbonization of the organic ligands and formation of nitrogen-doped graphitic carbon. The Zn species got removed at the give temperature, giving rise to the formation of GPC.

S1.3. Instrumentation

The structural and phase information of the synthesized materials was analyzed using powder X-ray diffraction (PXRD) on an Empyrean diffractometer (Malvern PANalytical) equipped with Cu Kα radiation (λ = 1.5406 Å). Data were collected over a 2θ range of 5°–80° with a

step size of 0.02° and scan rate of 4° min^{-1}. Nitrogen adsorption–desorption measurements were carried out at 77 K using an Autosorb-iQ XR analyzer (Quantachrome Instruments) to determine the Brunauer–Emmett–Teller (BET) surface area and pore size distribution. Prior to measurements, samples were degassed under vacuum at 100 °C for 12 h. The morphology and surface texture of the materials were examined using field emission scanning electron microscopy (FESEM, JSM-7800F, JEOL), while the internal structure and nanoscale features were probed using high-resolution transmission electron microscopy ((HR)TEM) on a FEI Tecnai TF20 microscope operated at 200 kV. Elemental mapping and spatial distribution of metal species were assessed via high-angle annular dark-field scanning transmission electron microscopy (HAADF-STEM) combined with energy-dispersive X-ray spectroscopy (EDX) using a TESCAN MAGNA instrument. X-ray photoelectron spectroscopy (XPS) was performed using an AXIS Supra instrument (Kratos Analytical Ltd.) equipped with a monochromatic Al Kα X-ray source (1486.6 eV) to evaluate surface composition and oxidation states. Raman spectra were recorded on a Renishaw inVia Micro Raman spectrometer (UK) using a 514 nm excitation laser to probe the graphitic characteristics and vibrational modes of the samples. Metal content and stoichiometry were quantified by inductively coupled plasma mass spectrometry (ICP-MS, Agilent 7900) after complete acid digestion of the materials.

S1.4. Electrochemical performance

Electrochemical characterization of the synthesized materials was performed using a standard three-electrode system in 1 M NaCl electrolyte. The working electrodes were prepared by dispersing 5 mg of the active material ($ZnCo_2O_4$@GPC) in a 1:1 mixture of deionized water and ethanol (1 mL), followed by ultrasonication for 30 minutes at room temperature. To enhance dispersion stability and improve adhesion, 35 μL of Nafion solution (5 wt%) was added, and the mixture was further sonicated for 10 minutes to obtain a homogeneous slurry. The ink was drop-cast onto a 1 cm^2 piece of Toray carbon paper and dried under ambient conditions, achieving an average mass loading of 1 mg cm^{-2}. Electrochemical measurements including cyclic voltammetry (CV), galvanostatic charge–discharge (GCD), and electrochemical impedance spectroscopy (EIS) were carried out on a Biologic VSP-3e potentiostat. Ag/AgCl (saturated KCl) and platinum foil were used as the reference and counter electrodes, respectively. CV measurements were conducted at various scan rates, and specific capacitance (C, F g^{-1}) was calculated using the integral form:

$$C = \frac{\int_{V_i}^{V_f} i\, dV}{2mv\,(V_f - V_i)}$$ ----------Eq(S1)

where i is the response current, ν is the scan rate, m is the mass of active material, and Vf and Vi are the final and initial potentials.

GCD tests were performed at different current densities, and specific capacitance was calculated as:

$$C = \frac{i\,\triangle t}{m\triangle v}$$ ----------Eq(S2)

where i is the constant current, Δt is the discharge time, and ΔV is the potential window.

S1.5. Flow capacitive deionization performance

FCDI experiments were performed using a symmetric flow-through cell to evaluate the desalination performance of $ZnCo_2O_4$@GPC. The flowable electrode was prepared by dispersing 3 g of $ZnCo_2O_4$@GPC and 0.5 g of NaCl in 100 mL of deionized water, followed by 8 hours of magnetic stirring and sonication to ensure uniform dispersion. The flow-electrode slurry was continuously circulated through both anode and cathode compartments using a peristaltic pump (Ravel Hiteks Pvt Ltd), while a 1.5 g L^{-1} NaCl feed solution was pumped through the spacer channel at a constant flow rate of 20 mL min^{-1}. A Biologic VSP-3e potentiostat was used to apply a constant voltage (typically 0.8 V) across the electrodes. The entire system was operated in a closed-loop configuration. Real-time conductivity of the effluent was recorded using a Mettler Toledo Five Easy Plus conductivity meter. Salt adsorption capacity (SAC, mg g^{-1}) and salt adsorption rate (SAR, mg g^{-1} min^{-1}) were calculated using:

$$Salt\ adsorption\ capacity = \frac{(C_i - C_f) \times V}{m}$$ ----------Eq(S3)

$$Salt\ adsorption\ rate = \frac{SAC}{t}$$ ----------Eq(S4)

where Ci and Cf are the initial and final NaCl concentrations, V is the volume of the feed, m is the mass of the active material in one electrode, and t is the desalination time.

Additional performance metrics were calculated as follows:

$$Salt\ removal\ (SR, \%) = \frac{(C_i - C_f) \times 100}{C_i}$$ ----------Eq(S5)

$$Charge\ efficiency(CE,\%) = \frac{SAC \times F \times m}{M \times \int i\ dt}$$ ----------Eq(S6)

$$ASRR(\mu mol\ cm^{-2} min^{-1}) = \frac{n\ (C_0 - C_f) \times V_s}{M \times A \times t}$$ ----------Eq(S7)

$$SEC(kWh/m^3) = \frac{\int i \times U\ dt}{(C_i - C_f) \times v}$$ ----------Eq(S8)

where F is the Faraday constant (96485 C mol^{-1}), M is the molar mass of NaCl (58.5 g mol^{-1}), U is the applied voltage, A is the electrode area, Vs is the flow rate, and v is the volume of treated water. FCDI performance was evaluated across varying feed concentrations (1.5–4.5 g L^{-1}), voltages (0.5–1.0 V), and long-term cycling to identify optimal operating conditions and assess stability.

S2. Structural and Morphological Characterizations

S2.1. FESEM analysis of Zn/Co-ZIF

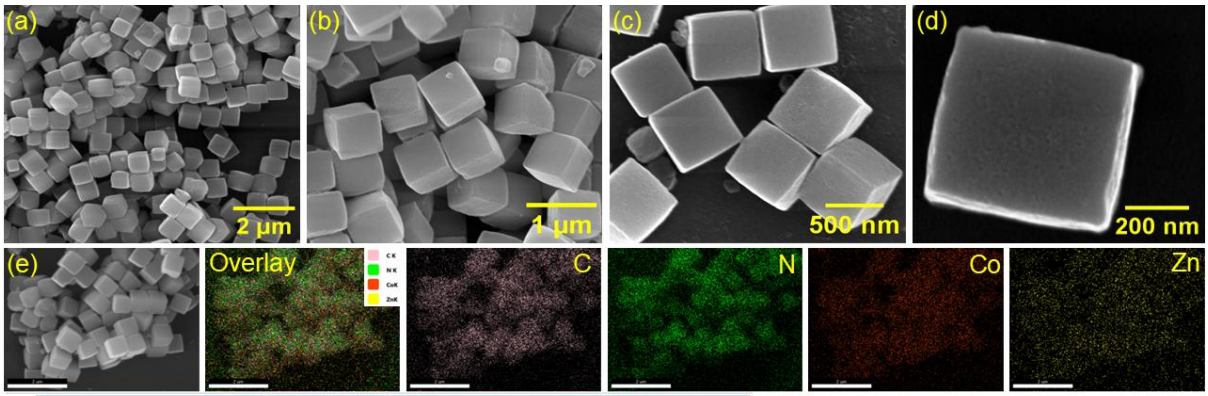

Element	Weight %	Atomic %	Error %
C K	24.8	34.7	6.1
N K	58.8	56.9	3.1
Co K	11.2	6.1	1.8
Zn K	5.2	2.3	1.3

Figure S1: FESEM and EDX analysis of Zn/Co-ZIF.

S2.2. FESEM analysis of Zn/CoNP@GPC

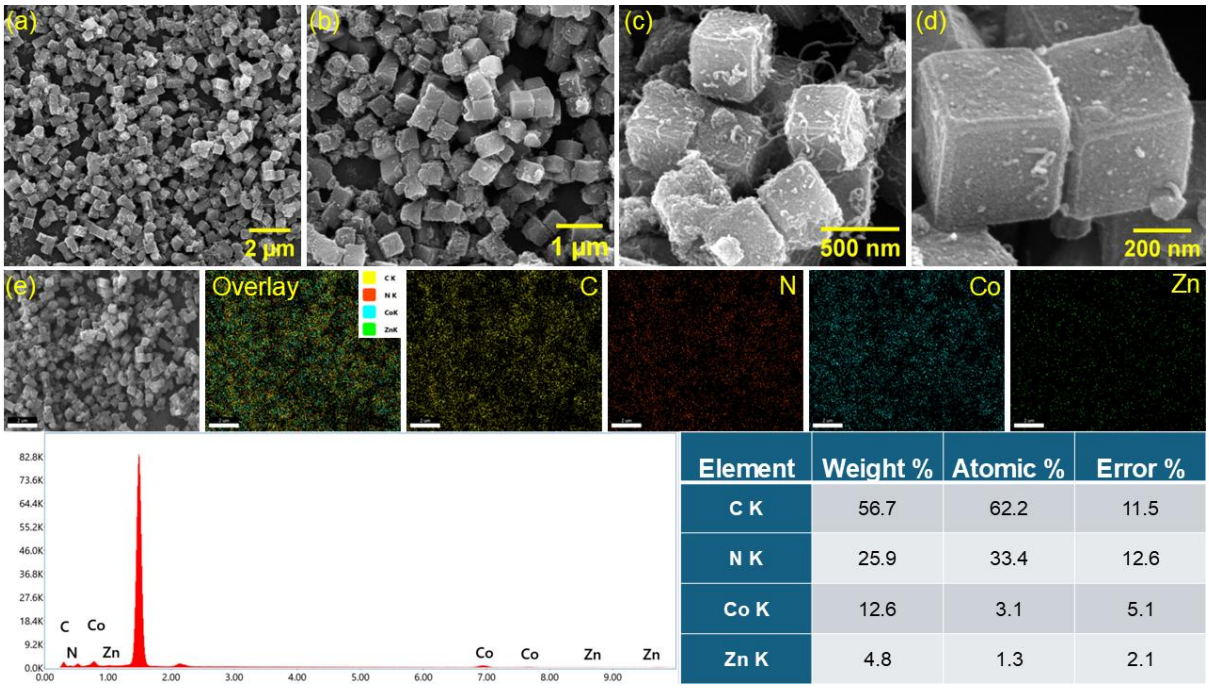

Element	Weight %	Atomic %	Error %
C K	56.7	62.2	11.5
N K	25.9	33.4	12.6
Co K	12.6	3.1	5.1
Zn K	4.8	1.3	2.1

Figure S2: FESEM and EDX analysis of Zn/CoNP@GPC.

S2.3. FESEM analysis of $ZnCo_2O_4$@GPC

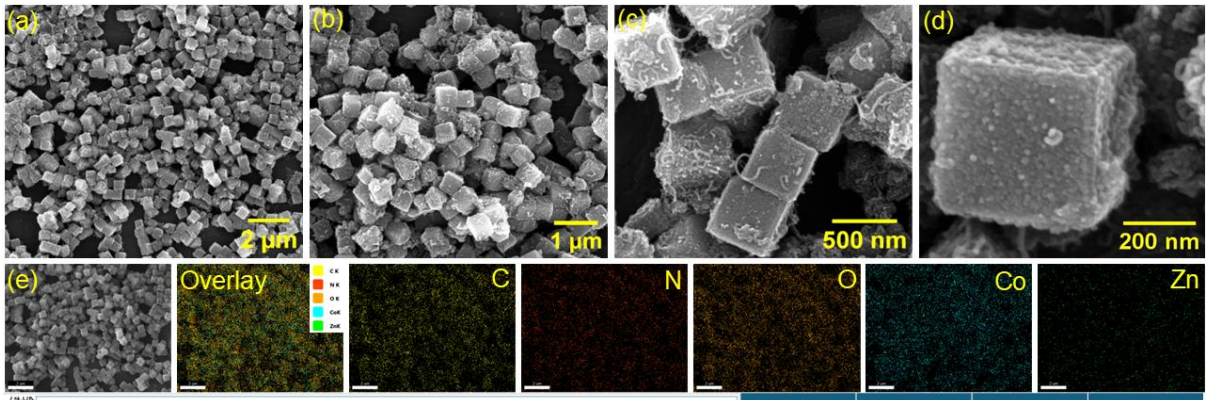

Element	Weight %	Atomic %	Error %
C K	35.1	56.5	11.8
N K	14.5	15.6	4.6
O K	30.1	20.3	7.5
Co K	14.6	5.4	2.8
Zn K	5.7	2.2	1.4

Figure S3: FESEM and EDX analysis of $ZnCo_2O_4$@GPC.

S2.4. HRTEM analysis of Zn/Co-ZIF

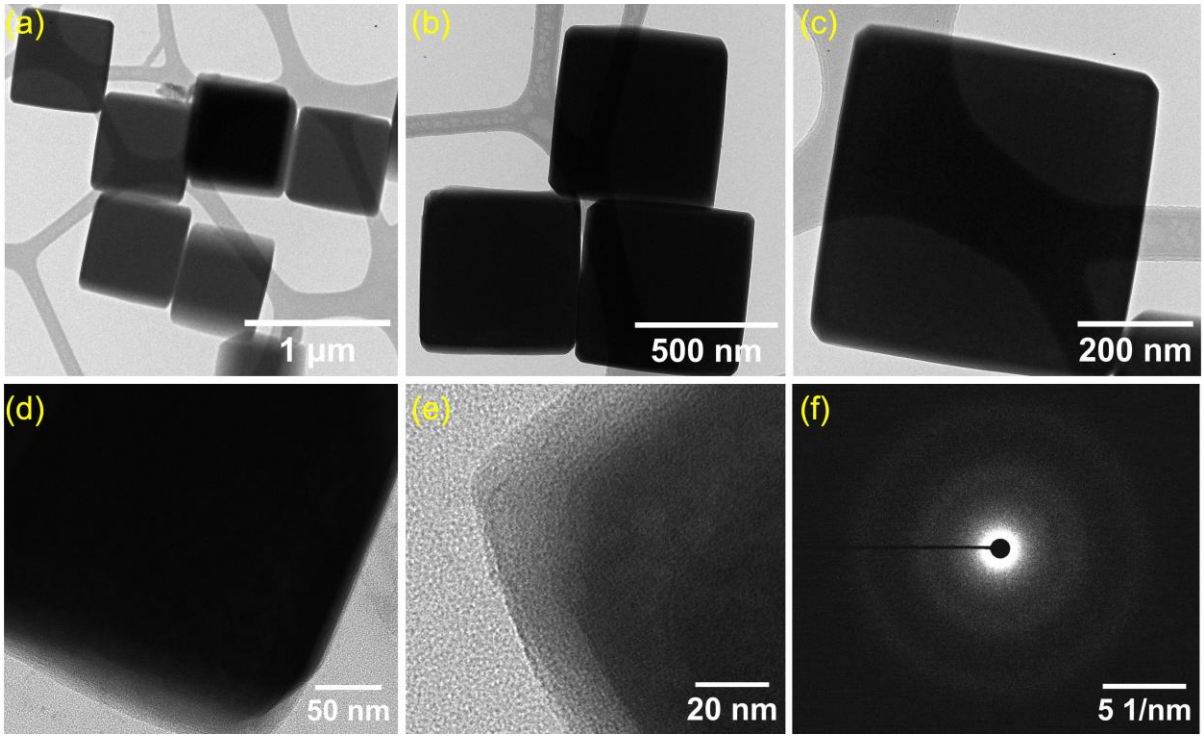

Figure S4: HRTEM analysis of Zn/Co-ZIF.

S2.5. HRTEM analysis of Zn/CoNP@GPC

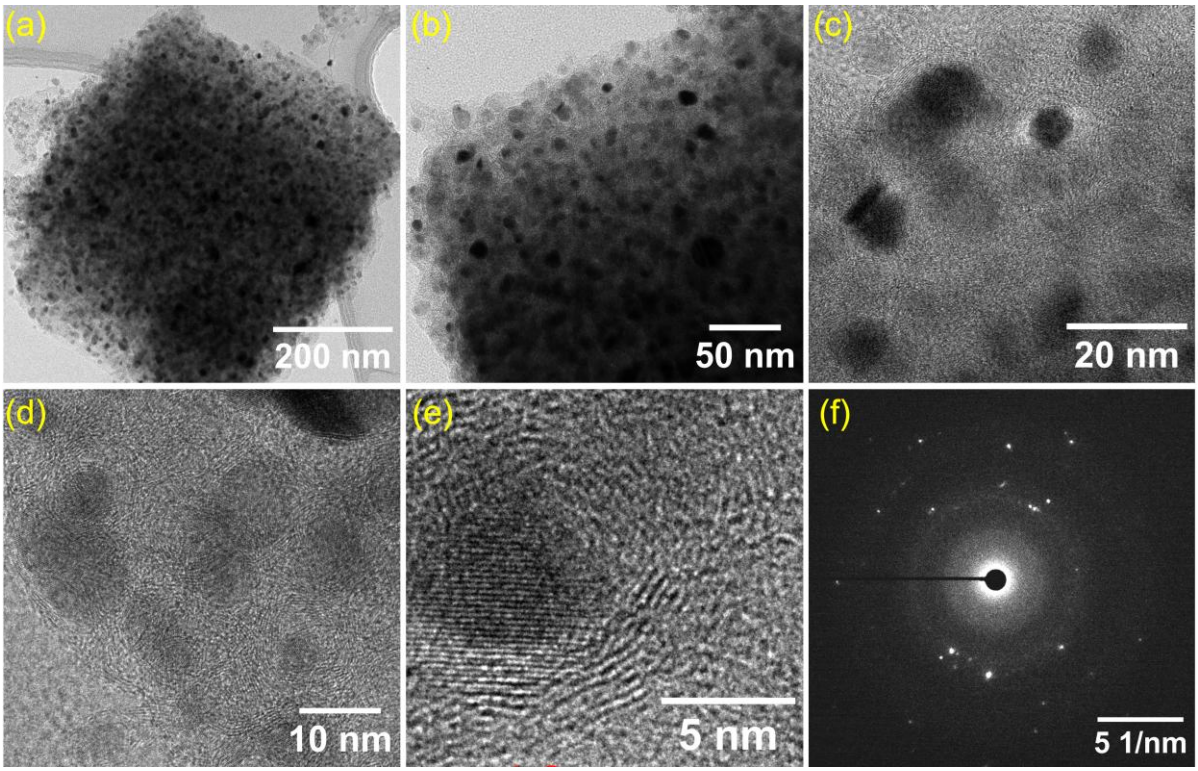

Figure S5: HRTEM analysis of Zn/CoNP@GPC.

S2.6. XPS survey spectra analysis comparison

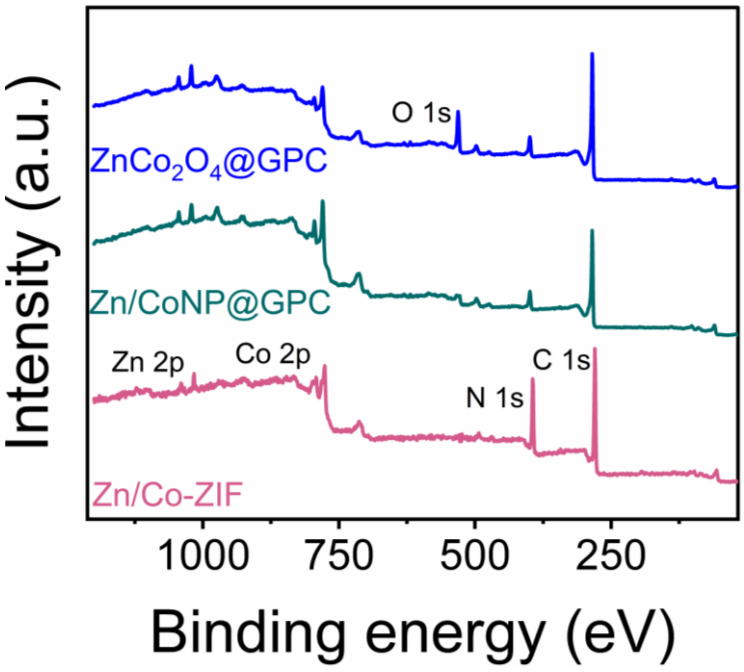

Figure S6: XPS survey spectra comparison of Zn/Co-ZIF, Zn/CoNP@GPC and $ZnCo_2O_4$@GPC

S3. Additional information about FCDI performance

S3.1. FCDI performance of Zn/CoNP@GPC

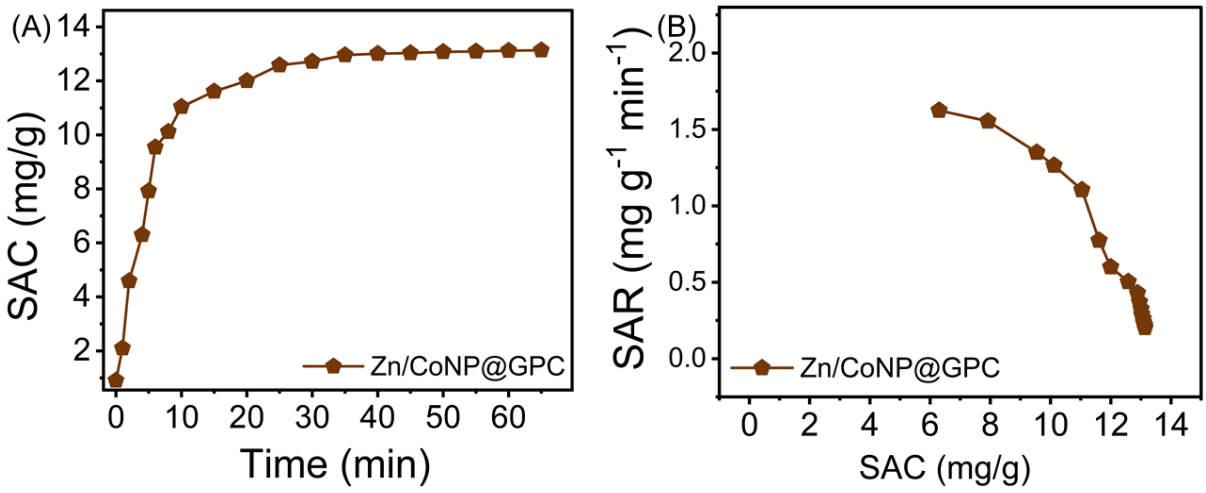

Figure S7: FCDI performance of Zn/CoNP@GPC. (A) Salt adsorption capacity at different time intervals at 0.8 V, (B) SAC vs SAR plot.

S3.2. XRD analysis and FCDI performance of Co_3O_4@GPC

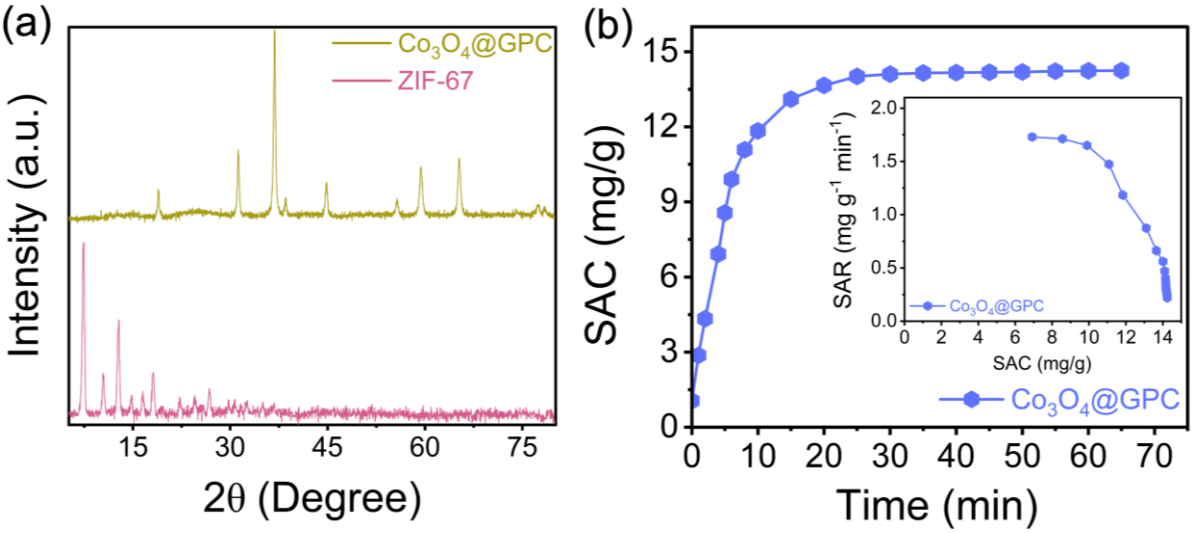

Figure S8: (A) PXRD patterns of Co_3O_4@GPC, (B) FCDI performance of Co_3O_4@GPC (inset: SAC vs SAR plot)

S3.3. Structural characterization, surface property and FCDI performance analysis of GPC and ZIF-8 and AC

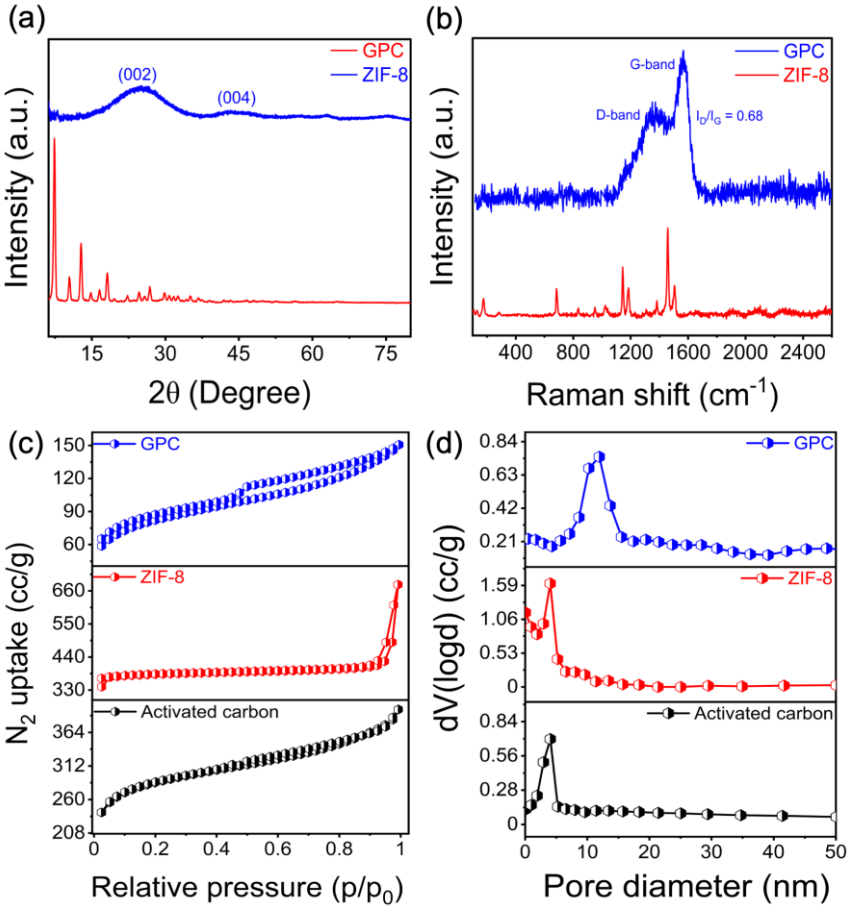

Figure S9: (a) XRD plot of ZIF-8 and derived GPC. (b) corresponding Raman spectra analyses. (c) BET adsorption isotherm for activated carbon, ZIF-8 and GPC. (c) corresponding pore size distribution obtained from NLDFT method.

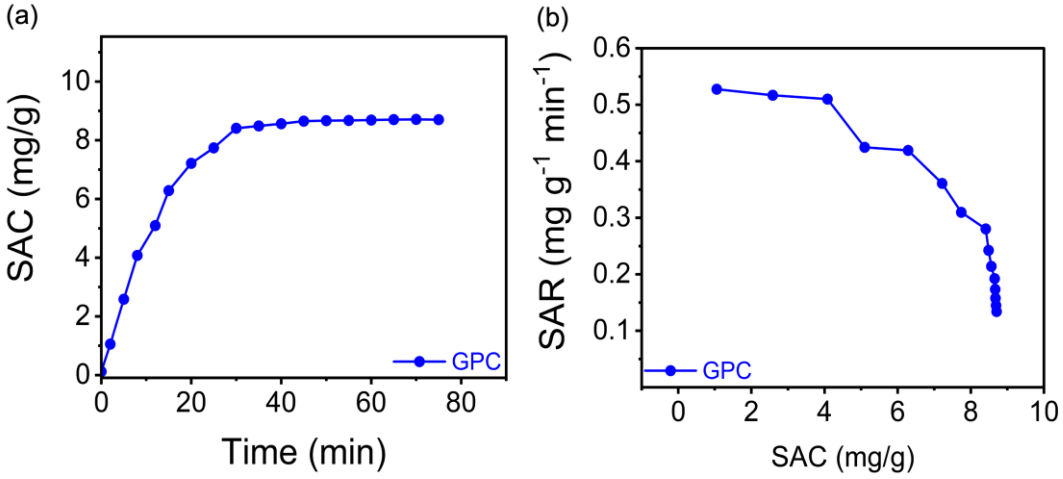

Figure S10: (a) SAC and (b) SAR plot for GPC.

S3.4. XRD analysis and FCDI performance analysis of $ZnCo_2O_4$, GPC and $ZnCo_2O_4$-GPC

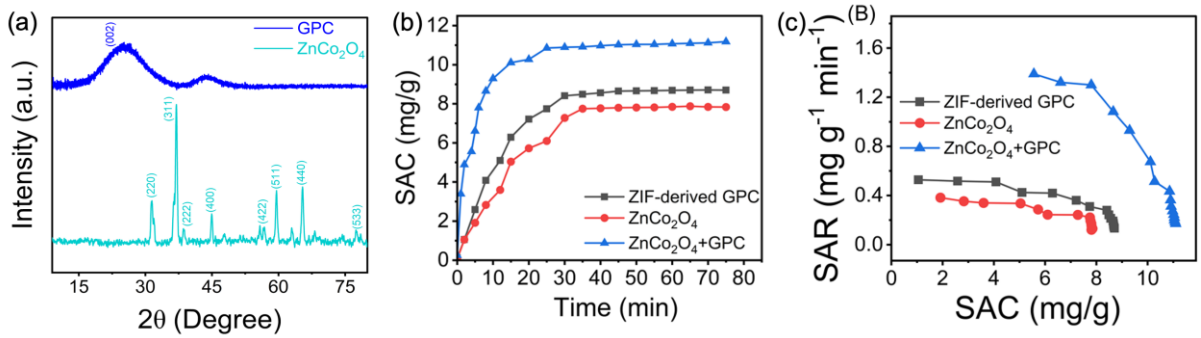

Figure S11: (a) XRD plot of $ZnCo_2O_4$ and GPC. (b) SAC and (c) SAR plot for all control samples.

S3.5. FCDI performance by varying applied potential

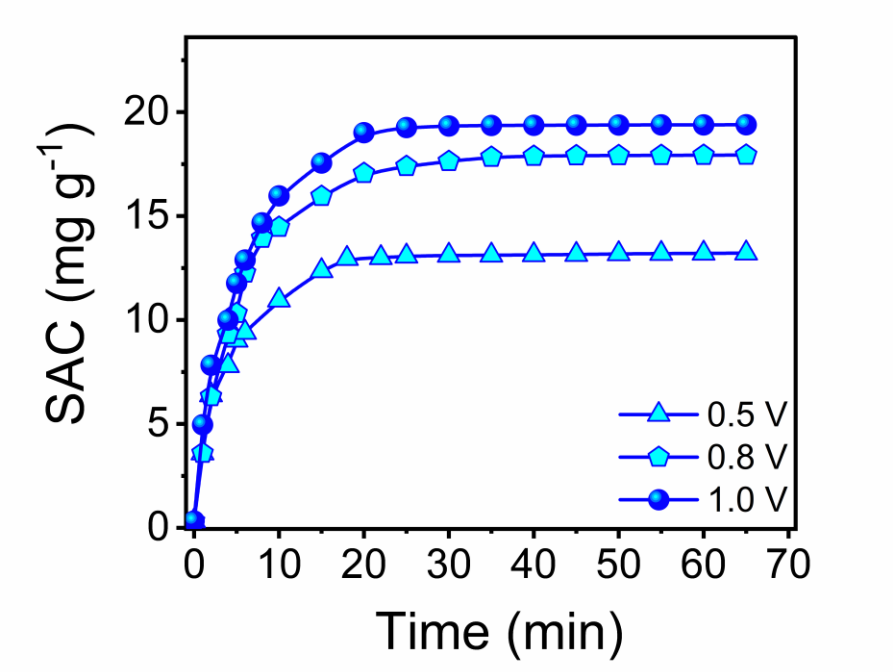

Figure S12: FCDI performance (SAC vs Time) at different applied potential

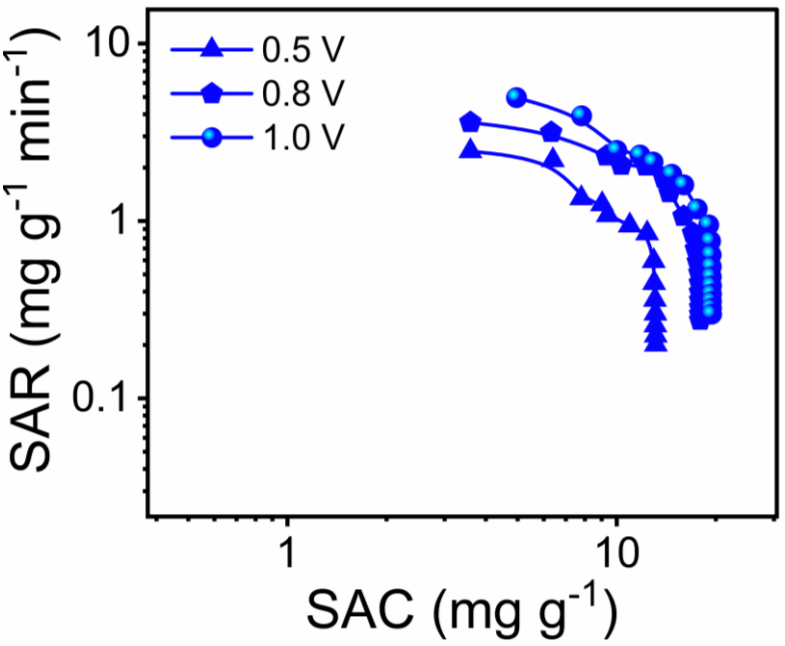

Figure S13: Corresponding Ragone plot at different applied potential

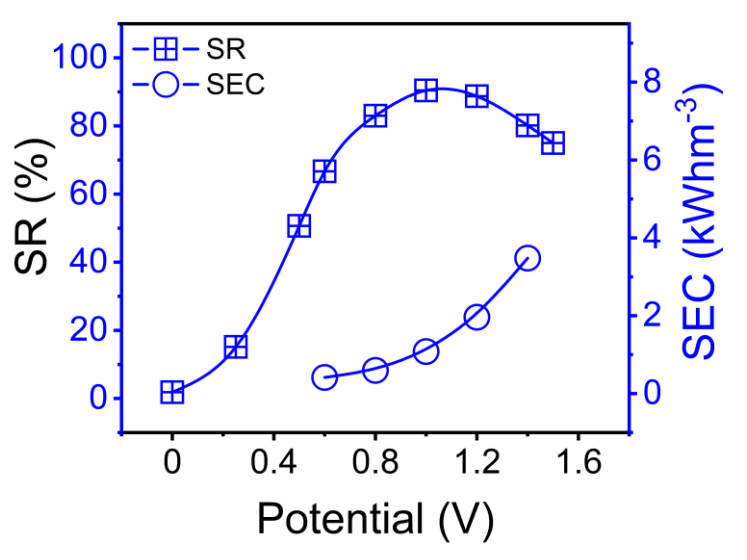

Figure S14: SR vs SEC plot with varying potential (Conditions: 1.5 g L^{-1} aqueous solution of NaCl and 20 mL min^{-1} flow rate).

S3.6. FCDI performance by varying feed salt concentration

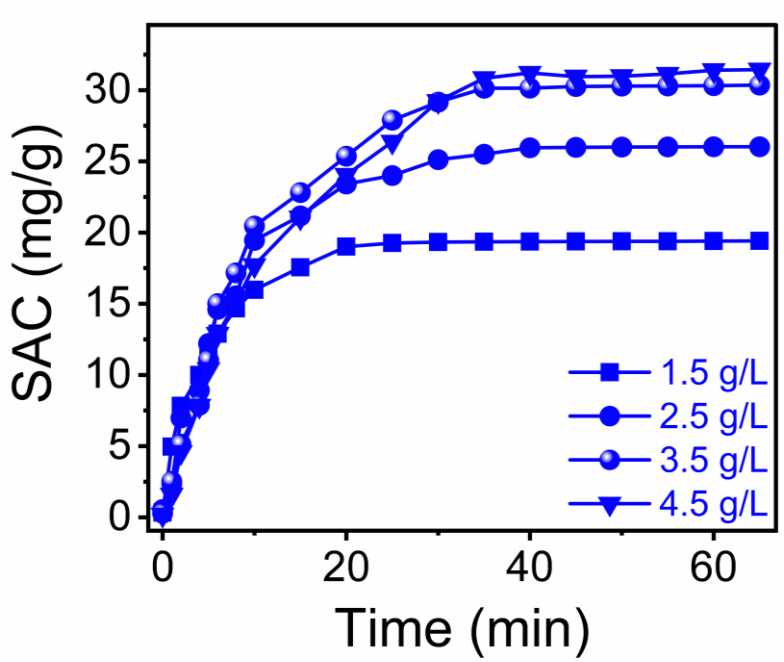

Figure S15: FCDI performance (SAC vs Time) by varying feed salinity (C_f) with 20 mL min^{-1} flow rate and 1.0 V potential)

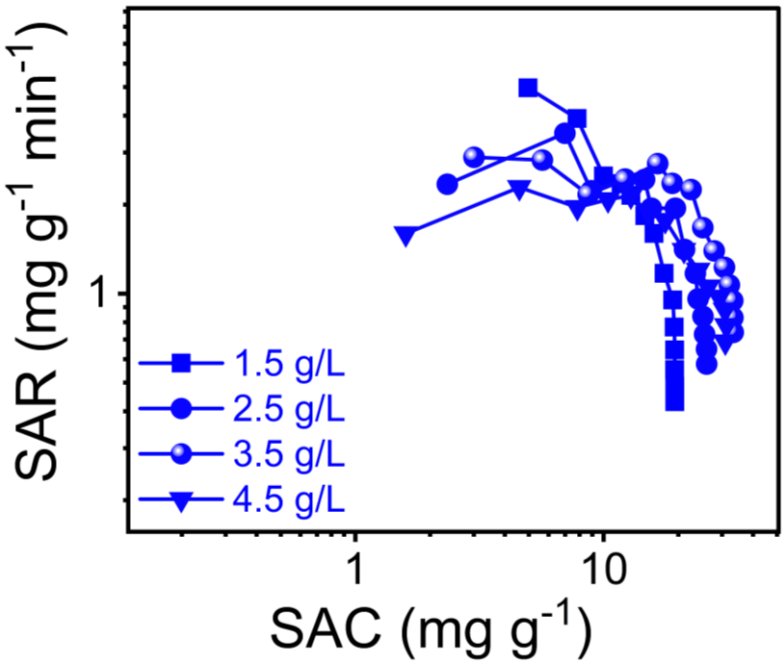

Figure S16: Corresponding Ragone plot for different feed concentrations

S3.7. EIS analysis of $ZnCo_2O_4$ and all control samples

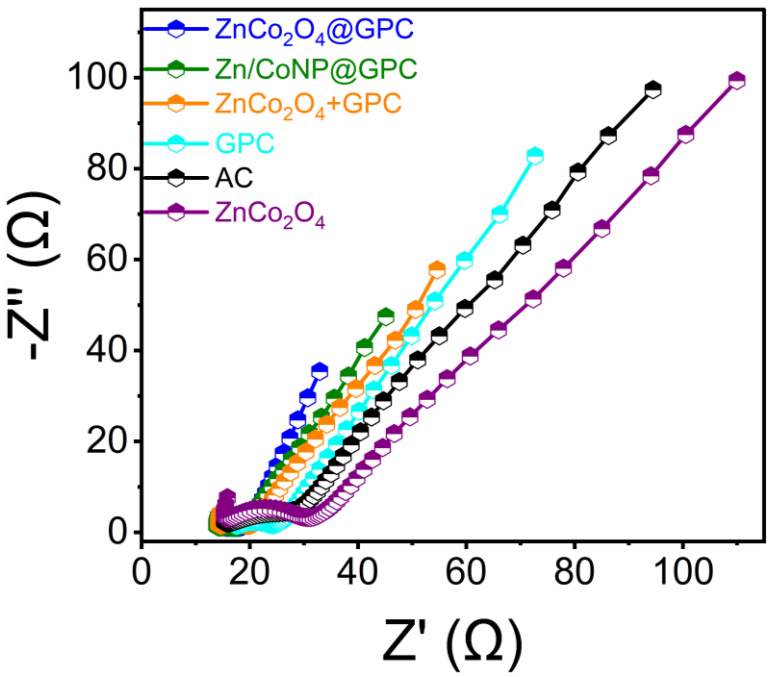

Figure S17: EIS analysis of all controlled samples in comparison to $ZnCo_2O_4$@GPC.

S4. Post-FCDI structural and morphological analysis

After the regeneration experiments, the $ZnCo_2O_4$@GPC flow electrodes were recovered by centrifugation, rinsed with DI water, and dried prior to characterization. FESEM and HRTEM analyses confirmed retention of the characteristic cubic morphology without structural collapse or agglomeration. XRD patterns of the regenerated samples remained identical to the pristine material, confirming the structural robustness and phase stability of the spinel framework. XPS revealed a slight positive binding energy shift for both Co 2p and Zn 2p, attributable to partial surface oxidation of the metal centers during extended cyclic deionization (Figure S11). The graphitic carbon phase was preserved, as evidenced by characteristic reflections in XRD and the C 1s envelope in XPS. Moreover, FESEM–EDS mapping showed negligible changes in morphology and elemental distribution, validating the compositional stability of the electrode after long-term cycling. Collectively, these results demonstrate the structural integrity, electronic stability, and durability of $ZnCo_2O_4$@GPC as a robust flow electrode for large-scale and sustained desalination applications.

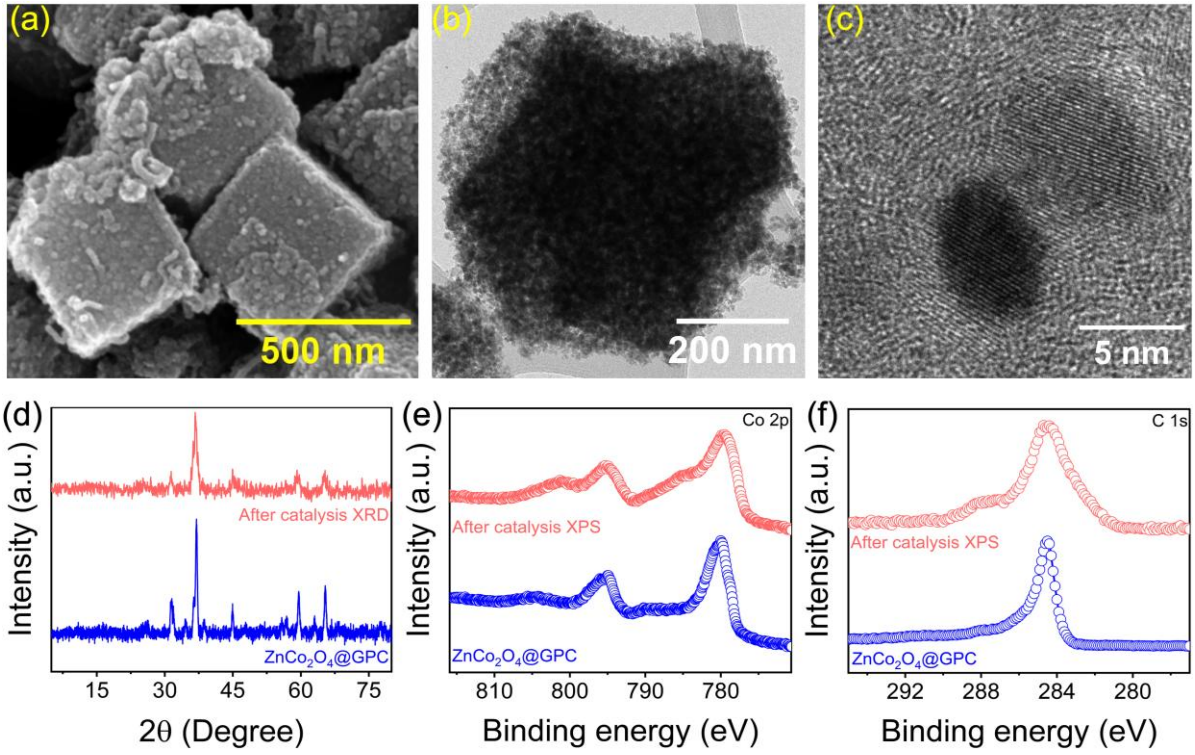

Figure S12: Morphological and structural analysis of $ZnCo_2O_4$@GPC (a) FESEM imaging. (b, c) HRTEM imaging. (d) comparative XRD analysis of before and after catalysis samples. (e, f) Co 2p and C1s XPS spectra comparison of before and after catalysis samples.

Table S1: Comparative study of the desalination performance of flow-electrode with previously reported literatures.

Electrode composition			Desalination capacity (mg g^{-1})	Desalination Rate	References
Electrode material	Effluent conc.				
FeOOH	500		22.06 at 1.2 V	---	[4]
NTP/rPGO	500 ppm		33.25 at 1.4V	1.8 mg g^{-1} min^{-1}	[5]
MoS_2/MXene	500 ppm		23.98 at 1.2V	4.6 mg g^{-1} min^{-1}	[6]
Na_2MnSiO_4/C (NMSO-1)	500 mg L^{-1}		31 at 1.2 V	---	[7]
rGO/Co_3O_4	500 ppm		18.63 at 1.6 V	3.12	[8]
RGO–PPy–Mn	500 mg L^{-1}		18.4 at 2.0 V	0.153 mg g^{-1} min^{-1}	[9]
o-OMC-800	584 mg L^{-1}		14.58 at 1.2 V	-----	[10]
MWCNT/PTFE	3000 mg L^{-1}		15.64 at 1. 0 V	-----	[11]
Graphene-Fe_3O_4	146 mg L^{-1}		10.34 at 1.6 V	-----	[12]
ZIF-67/PPy	584 mg L^{-1}		11.85 at 1.2 V	~2 mg g^{-1} min^{-1}	[13]
ZIF-8@PZS-C	500 mg L^{-1}		22.19 at 1.2 V	------	[14]
PSS-AGA	1000 mg L^{-1}		26.33 at 1.4 V	------	[15]
OMCF	500 mg L^{-1}		12.17 at 1.2 V	3.3 mg g^{-1} min^{-1}	[16]
$ZnCo_2O_4$@GPC	3500 mg L^{-1}		22.06 at 1.2 V	3.1 mg g^{-1} min^{-1}	This work

References:

(1) K. Zhou, B. Mousavi, Z. Luo, S. Phatanasri, S. Chaemchuen, F. Verpoort, J. Mater. Chem. A 2017, 5, 952-957.

(2) S. Biswal, B. Mishra, B. P. Tripathi, Small 2026, n/a, e10645.

(3) L. Zhang, Z. Su, F. Jiang, L. Yang, J. Qian, Y. Zhou, W. Li, M. Hong, Nanoscale 2014, 6, 6590-6602.

(4) J. Zhao, B. Wu, X. Huang, Y. Sun, Z. Zhao, M. Ye, X. Wen, Adv. Sci. 2022, 9, 2201678.

(5) C. Han, Q. Meng, B. Cao, G. Tian, ACS Omega 2019, 4, 11455-11463.

(6) Z. Chen, X. Xu, Y. Liu, J. Li, K. Wang, Z. Ding, F. Meng, T. Lu, L. Pan, Desalination 2022, 528, 115616.

(7) Z. Chen, X. Zhang, W. Geng, C. Gong, Z. Li, C. Chen, Y. Zhang, G. Wang, J. Colloid Interface Sci. 2024, 662, 627-636.

(8) G. Divyapriya, K. K. Vijayakumar, I. Nambi, Desalination 2019, 451, 102-110.

(9) X. Gu, Y. Yang, Y. Hu, M. Hu, J. Huang, C. Wang, J. Mater. Chem. A 2015, 3, 5866-5874.

(10) X. Xu, H. Tan, Z. Wang, C. Wang, L. Pan, Y. V. Kaneti, T. Yang, Y. Yamauchi, Environmental Science: Nano 2019, 6, 981-989.

(11) N. Zouli, Journal of Saudi Chemical Society 2021, 25, 101328.

(12) X. Gu, M. Hu, Z. Du, J. Huang, C. Wang, Electrochim. Acta 2015, 182, 183-191.

(13) Z. Wang, X. Xu, J. Kim, V. Malgras, R. Mo, C. Li, Y. Lin, H. Tan, J. Tang, L. Pan, et al., Materials Horizons 2019, 6, 1433-1437.

(14) J. Zhang, J. Fang, J. Han, T. Yan, L. Shi, D. Zhang, J. Mater. Chem. A 2018, 6, 15245-15252.

(15) A. G. El-Deen, H. K. El-kholly, M. E. M. Ali, H. S. Ibrahim, M. K. Zahran, M. H. Helal, J.-H. Choi, Sep. Purif. Technol. 2022, 299, 121760.

(16) L. Zhang, R. Wang, W. Chai, M. Ma, L. Li, ACS Appl. Mater. Interfaces 2023, 15, 48800-48809.